Supplementary information

Self-healing electronic skin with high fracture strength and toughness

Jaehoon Jung,[1] Sunwoo Lee,[1] Hyunjun Kim,[2] Wonbeom Lee, [1] Jooyeun Chong,[1] Insang You,[3]* and Jiheong Kang[2]*

[1] Department of Materials Science and Engineering, Korea Advanced Institute of Science and Technology (KAIST), Daejeon, 34141 Republic of Korea

[2] Department of Chemistry, Seoul National University, Seoul, 08826 Republic of Korea

[3] Department of Chemistry, University of Waterloo, 200 University Ave W., Waterloo, Ontario N3L3G1, Canada

*To whom correspondence should be addressed:

E-mail: jiheongkang@snu.ac.kr (J. K.) iyou@uwaterloo.ca (I.Y.)

Table of contents:

Supplementary Figure 1. Synthetic route to SHPs with different ratio of UPy and aromatic disulfide. SHP-1: n = 0.6, SHP-2: n = 0.8
Supplementary Figure 2. Synthetic route to SHP-3.
Supplementary Figure 3. ^{1}H NMR spectrums of SHPs in DMSO (400 MHz).
Supplementary Figure 4. GPC profiles of SHPs.
Supplementary Figure 5. Synthesis of UPy.
Supplementary Figure 6. Comparison of polymer and ionic conductor in S-S curve.
Supplementary Figure 7. Master curves of Self-healing materials.
Supplementary Figure 8. DSC data of self-healing materials.
Supplementary Figure 9. Fracture tests of self-healing materials.
Supplementary Figure 10. Stress-strain curves of self-healing materials.
Supplementary Figure 11. Cyclic tests of self-healing materials.
Supplementary Figure 12. Nyquist plot for SHIC-1 as a function of the amount of ionic liquid and the stress-strain curve (S-S curve) for SHIC-1 with 30 wt% EMIMTFSI.
Supplementary Figure 13. Self-healing tests of materials.
Supplementary Figure 14. Self-healing tests of SHIC-1.
Supplementary Figure 15. Self-healing stretchable multimodal sensor and electrodes.
Supplementary Figure 16. SEM image of self-healing artificial multimodal sensor.
Supplementary Figure 17. A comparison between self-healing artificial multimodal sensors with different active layers.
Supplementary Figure 18. Comparison of the temperature sensitivity of the multimodal sensor based on the amount of EMIMTFSI in the SHIC-1 active layer.
Supplementary Figure 19. Charge relaxation frequency behavior under different temperatures.
Supplementary Figure 20. Strain-insensitive temperature sensing under various temperature and strain.
Supplementary Figure 21. Charge relaxation frequency and capacitance behavior under stretching.
Supplementary Figure 22. Temperature-insensitive strain sensing under various temperatures and strains.
Supplementary Figure 23. Comparison of bode plots between pristine multimodal sensor and self-healed multimodal sensor.
Supplementary Figure 24. Difference in self-healing speed between the self-healing multimodal sensor and the self-healing damage sensor.
Supplementary Figure 25. Changes of resistance of flexion sensor as a function of strain.
Supplementary Figure 26. Cyclic test of the flexion sensor.
Supplementary Figure 27. The configuration of soft grippers.
Supplementary Figure 28. Actuation ability of the self-healing gripper.
Supplementary Figure 29. Bending soft pneumatic actuator for soft gripper applications.
Supplementary Figure 30. Self-healing stretchable flexion sensor and damage sensor.
Supplementary Figure 31. Sensory systems of the soft robot.
Supplementary Figure 32. Difference in resistance change of the self-healing damage sensor when grabbing an object versus when damage is inflicted.
Supplementary Table 1. Comparison of the ionic conductivity and mechanical toughness of ionic conductors mentioned in the references.

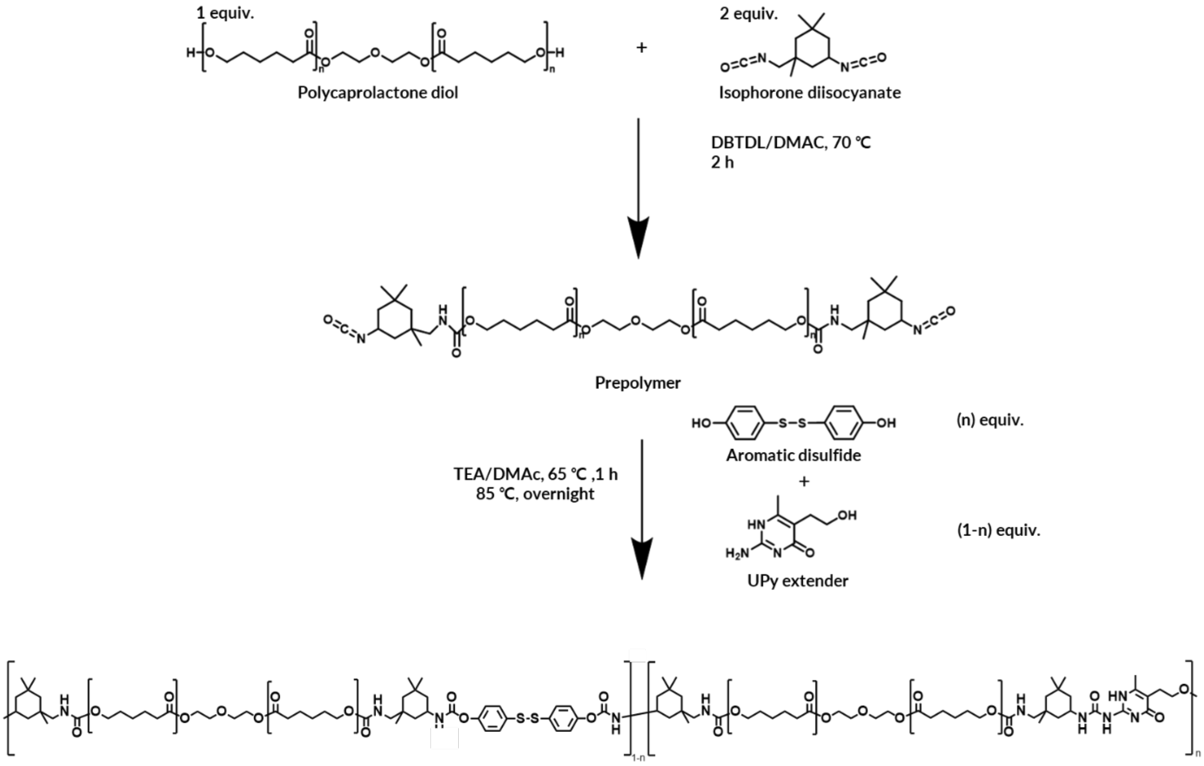

Supplementary Figure 1. Synthetic route to SHPs with different ratio of UPy and aromatic disulfide. SHP-1: n = 0.6, SHP-2: n = 0.8

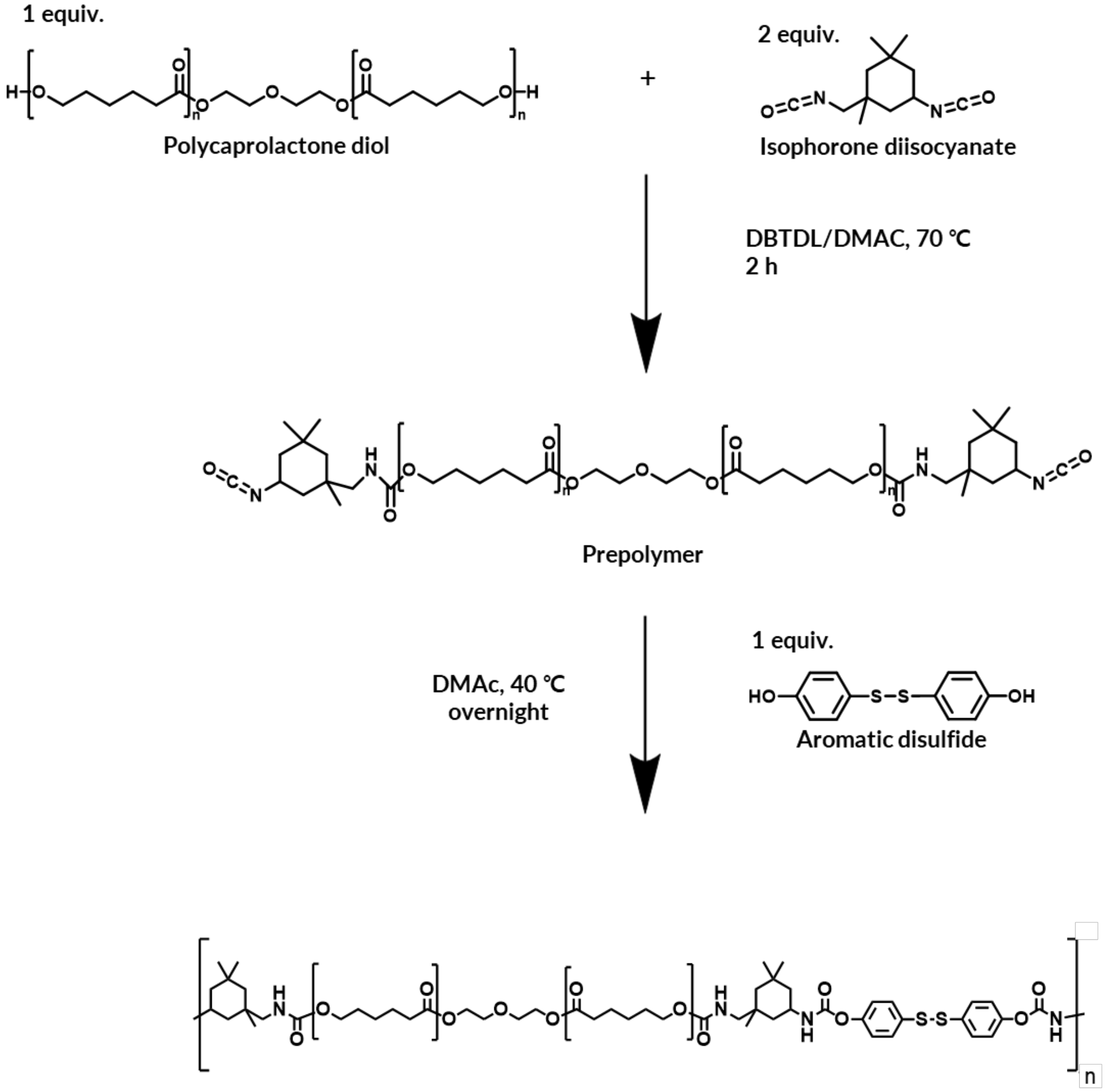

Supplementary Figure 2. Synthetic route to SHP-3.

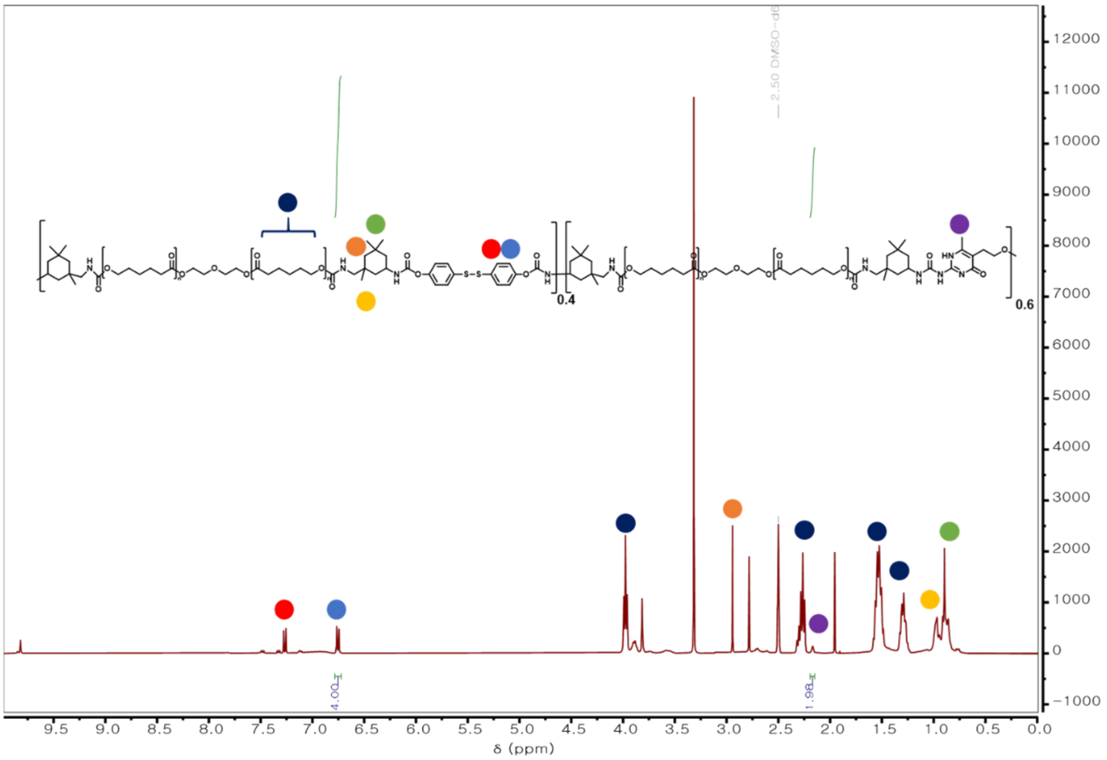

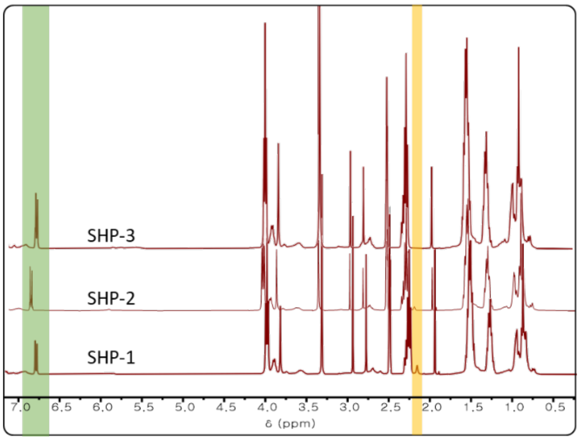

Polymer	# of Disulfide unit / # of UPy unit	
	Theoretical	Experimental
SHP-1	1.500	1.515
SHP-2	4.000	3.947
SHP-3	N.A.	N.A

Supplementary Figure 3. ^{1}H NMR spectrums of SHPs in DMSO (400 MHz).

In the ^{1}H NMR spectrums of SHPs, the peaks of disulfide aromatic unit appeared at 7.4~7.0 and 7.0~6.5 ppm. The peaks of protons adjacent to ester C-O in polycaprolactone appeared at 4.0 ppm, and those adjacent to ester C=O appeared at 2.3-2.2 ppm, respectively, indicating that soft segment is composed of polycaprolactone diol. Methylene protons appeared at 1.7~1.3 ppm and methyl (-CH_3) protons of isophorone diisocyanate appeared at 1.0~0.8 ppm, proton of urethane unit appeared at 3.0~2.8 ppm, and methyl protons adjacent to urethane unit appeared at 0.9~1.0 ppm suggesting that hard segment is composed of isophorone diisocyanate. Finally, methyl of UPy protons appeared at 2.2~2.0 ppm, and N-H proton of Upy appeared at 10.0~9.5 ppm. The ratio of disulfide unit and UPy in ^{1}H NMR corresponds to the ideal ratio of those.

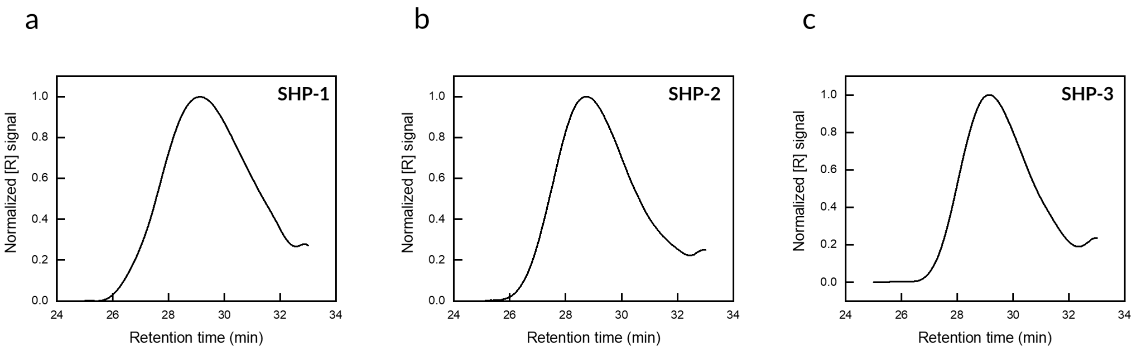

Supplementary Figure 4. GPC profiles of SHPs.

a, SHP-1. (Mn=14190 g/mol, Mw=52380 g/mol) **b,** SHP-2. (Mn=15150 g/mol, Mw=39530 g/mol) **c,** SHP-3. (Mn=12170 g/mol, Mw=25430 g/mol)

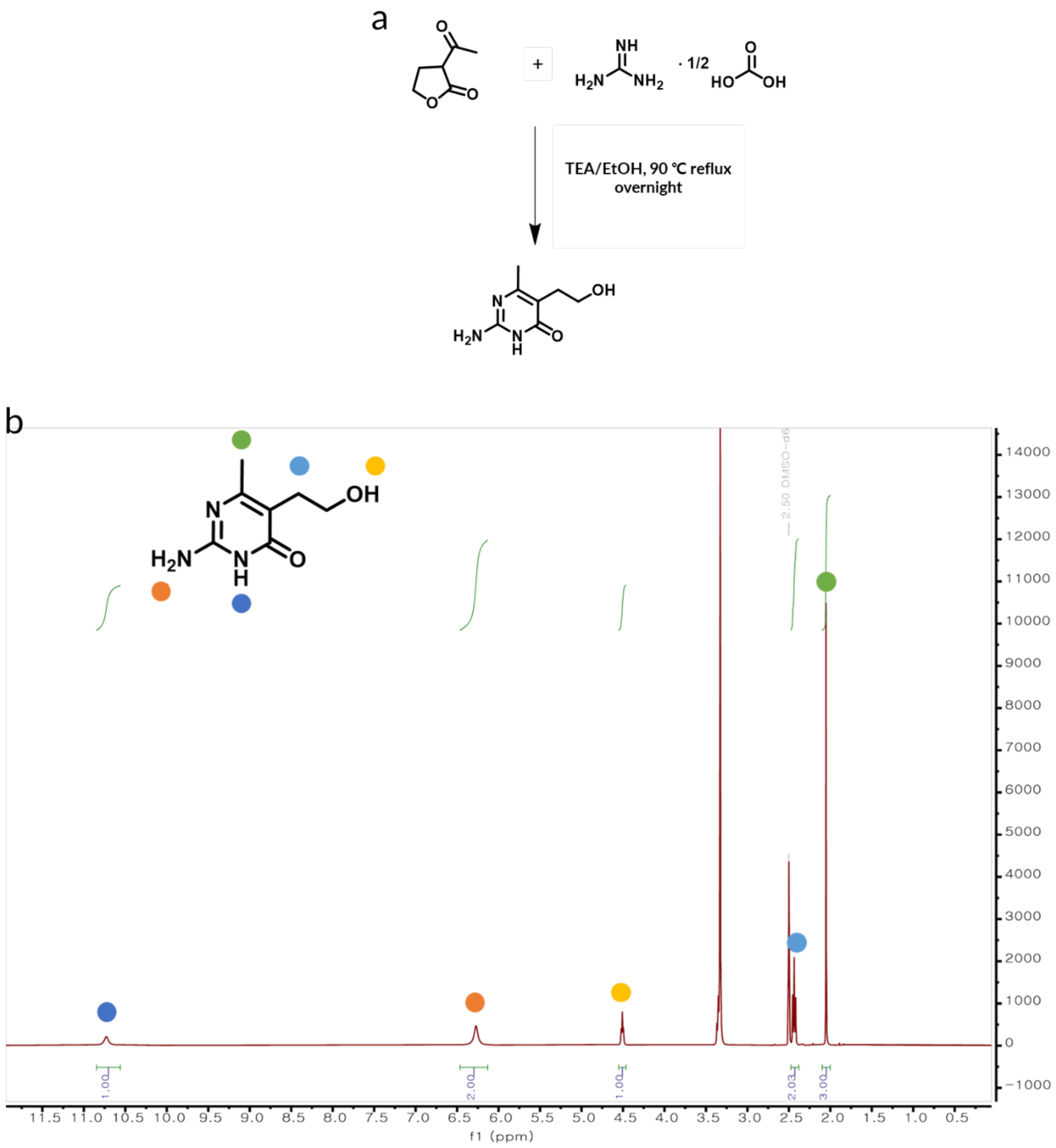

Supplementary Figure 5. Synthesis of UPy.

a, Synthetic route to UPy. **b,** 1H NMR spectrum of UPy in DMSO (400 MHz).: δ 2.02 (s, 3 H, 4-CH3), 2.43 (t, 2 H, J), 3.30 (t, 2 H, J), 4.51 (s, 1 H, OH, exch), 6.30 (s, 2 H, 2-NH2, exch), 10.75 (s, 1 H, 3-NH, exch).

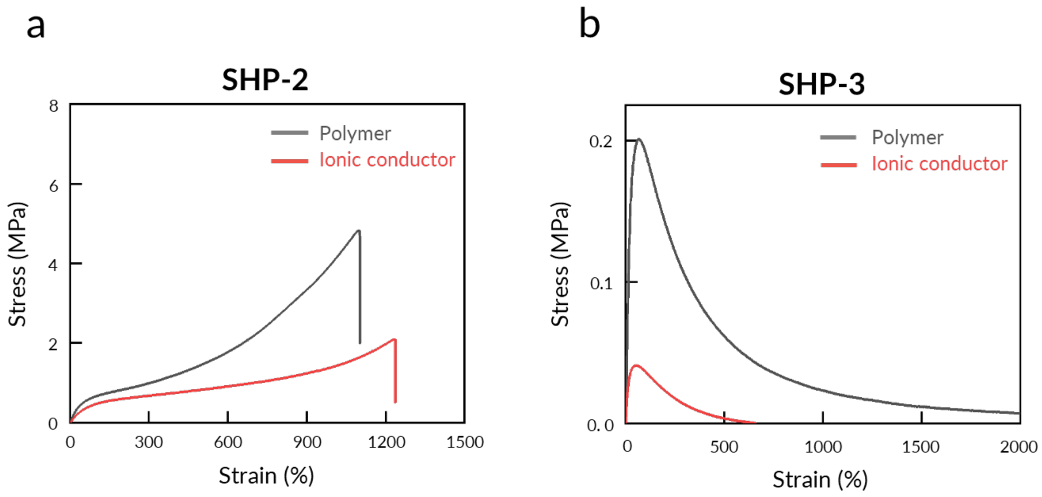

Supplementary Figure 6. Comparison of polymer and ionic conductor in S-S curve.

a, Comparison of SHP-2 and SHIC-2 in S-S curve. **b,** Comparison of SHP-3 and SHIC-3 in S-S curve. When ionic liquid was put into SHP, mechanical property of ionic conductor with more ratio of UPy was decreased less.

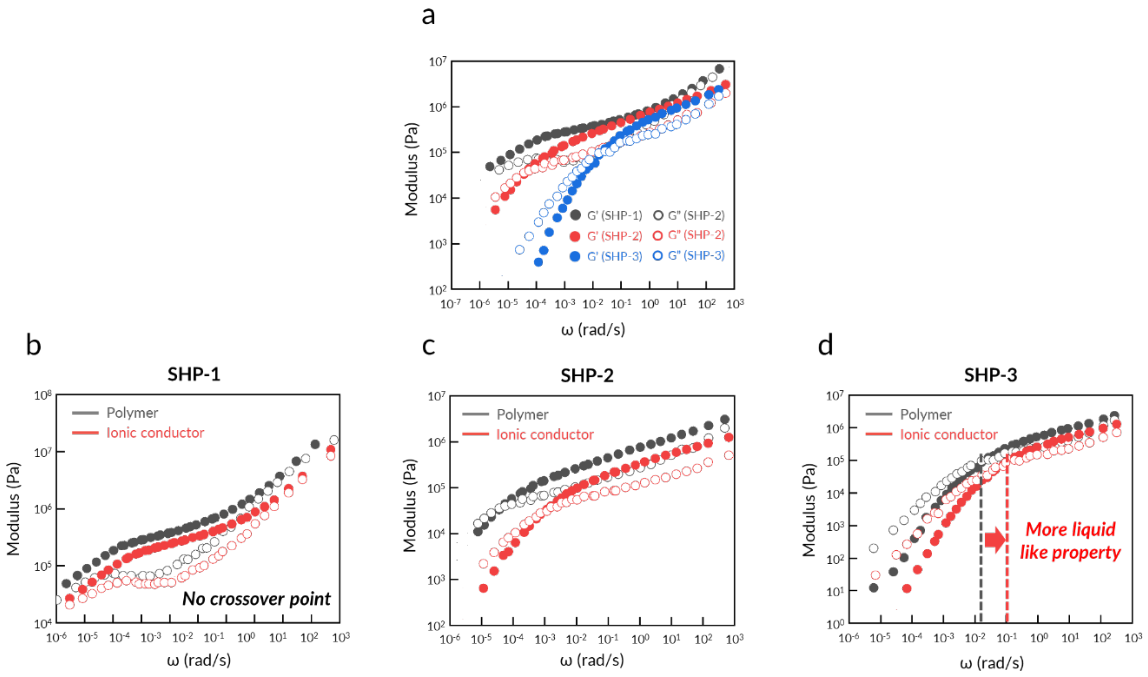

Supplementary Figure 7. Master curves of self-healing materials.

a, Mater curves of self-healing polymers. As the UPy content of the polymer increase, crossover frequency is lower, indicating that polymers with more UPy contents have more solid-like properties. **b-d,** Master curves of polymer and ionic conductor.

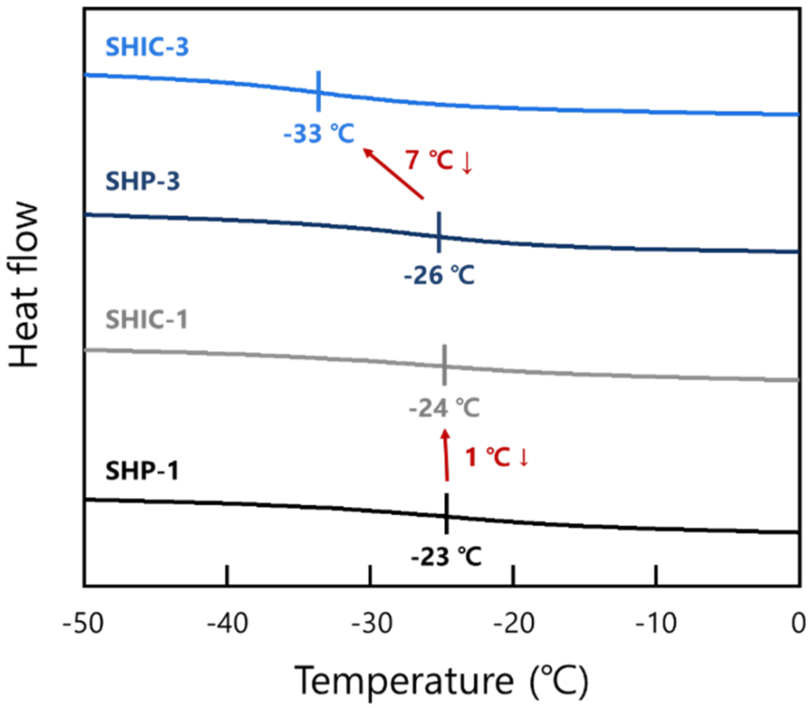

Supplementary Figure 8. DSC data of self-healing materials.

In the case of SHP-1 containing UPy moiety, the addition of ionic liquid does not significantly affect the chain mobility, resulting in little to no change in the glass transition temperature (T_g). In contrast, for SHP-3 lacking the UPy moiety, the addition of ionic liquid disrupts the inter-chain interactions, thereby increasing chain mobility and leading to a decrease in the T_g value.

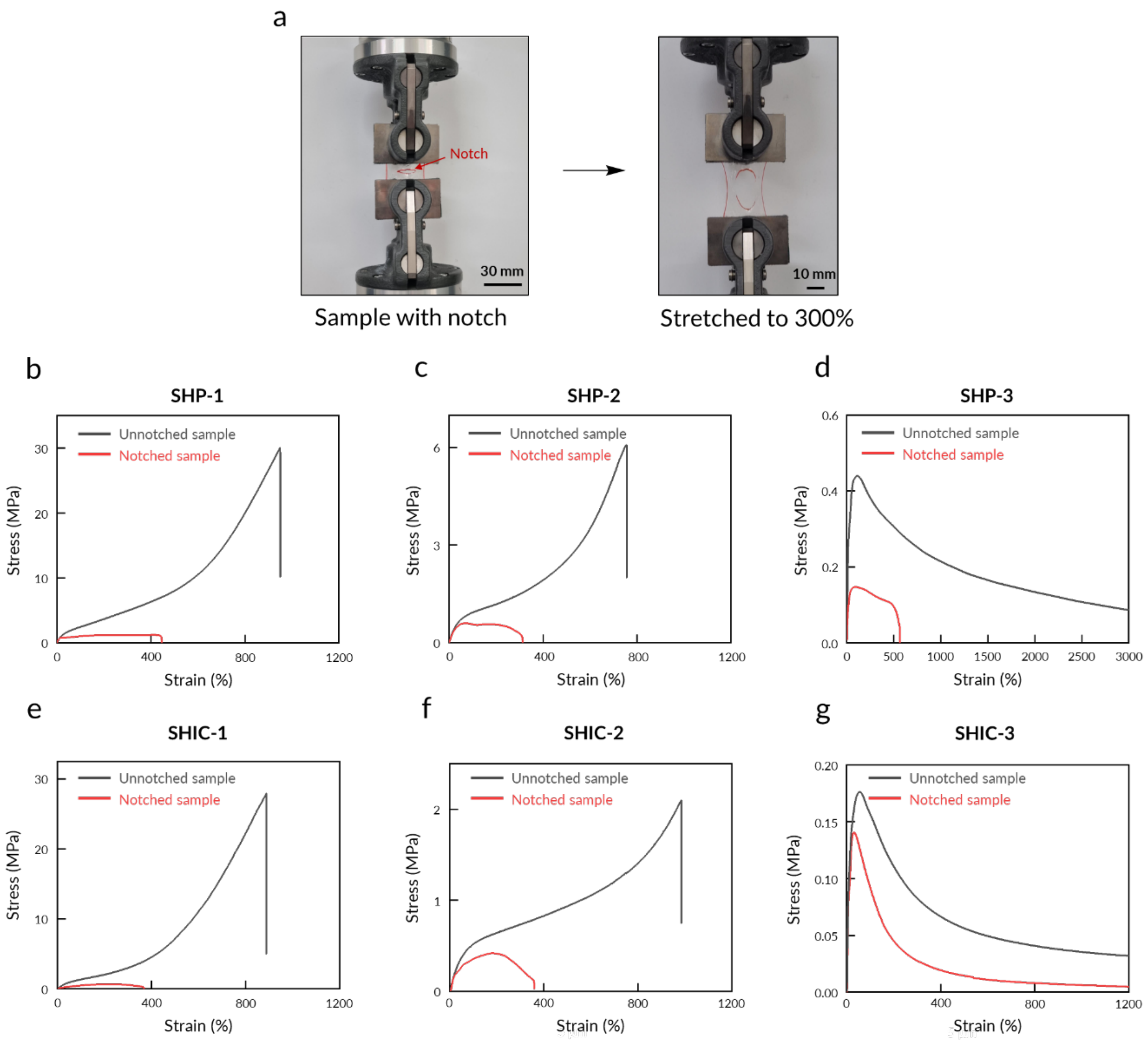

Supplementary Figure 9. Fracture tests of self-healing materials.

a, A notched SHIC-1 film before stretching (left) and after 300% stretching (right) in an Instron machine showing that the film is resistant to notch. **b-d,** Stress-extension curves of the unnotched and notched SHP. **e-g,** Stress-extension curves of the unnotched and notched SHIC.

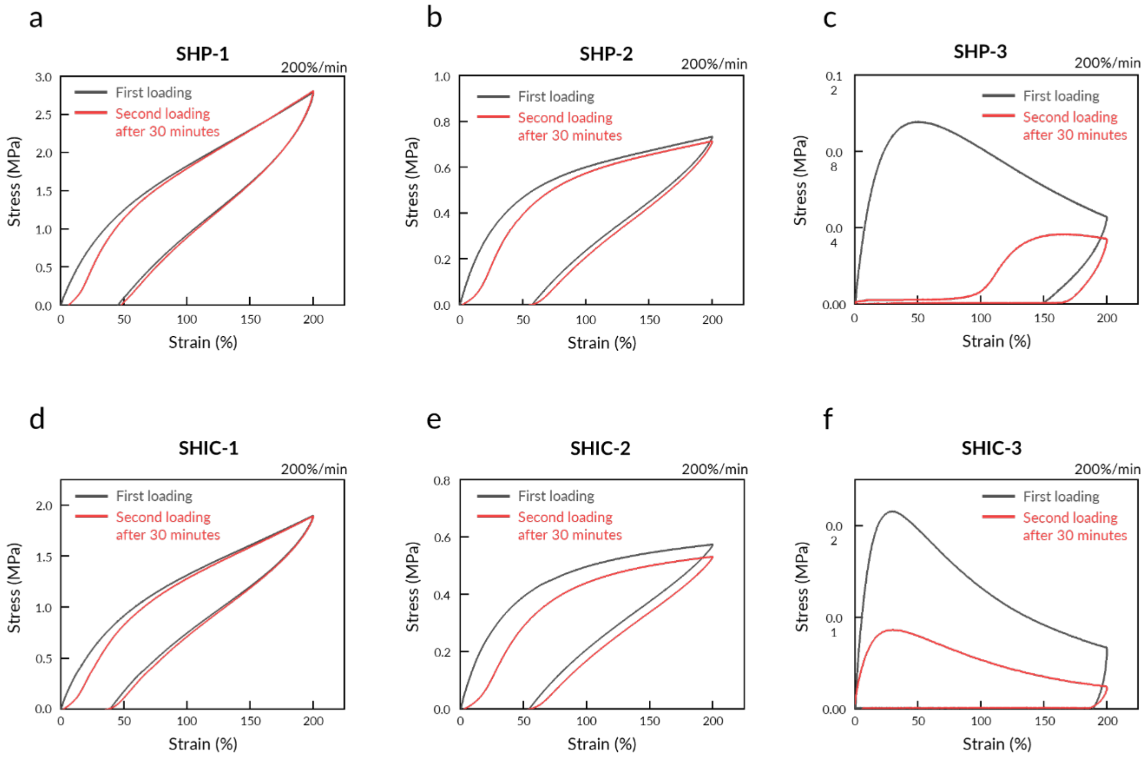

Supplementary Figure 10. Stress-strain curves of self-healing materials.

a-c, Cyclic stress-strain curves (up to 200% strain) of self-healing polymers at first loading (black) and second loading (red) after 30 minutes rest. SHP-1 and SHP-2 showed complete recovery thanks to strong H-bonding of UPy. SHP-3 which only have aromatic disulfide couldn't be recovered. **d-f,** Cyclic stress-strain curves (up to 200% strain) of self-healing polymers at first loading (black) and second loading (red) after 30 minutes rests. Only SHIC-1 showed complete recovery, because ionic liquid couldn't penetrate quadruple H-bonding.

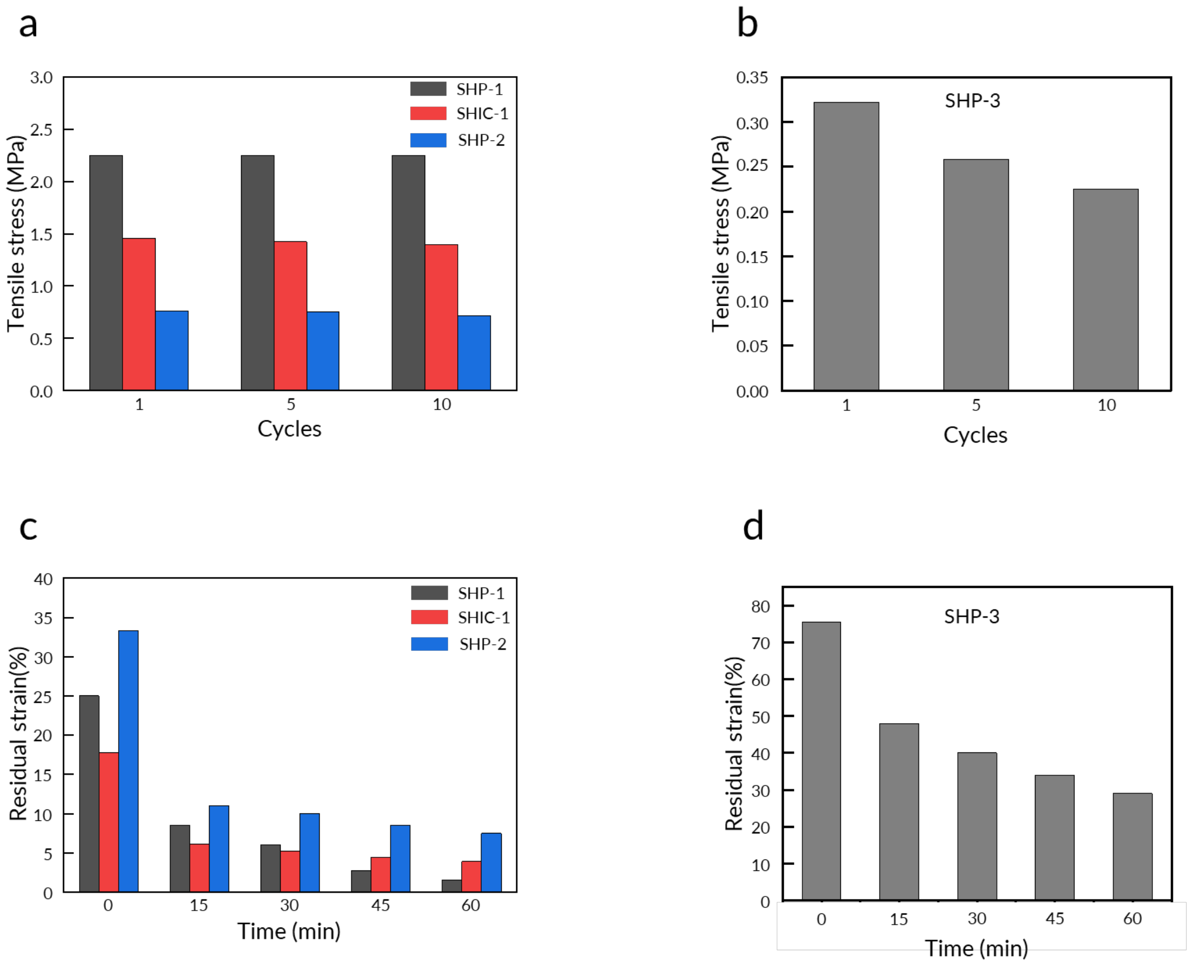

Supplementary Figure 11. Cyclic Tests of self-healing materials.

a, Tensile stress of self-healing materials at 100% strain with multiple cycles at 1000%/min with 15 minutes resting in between. Self-healing materials for robust self-healing robot were completely recovered. **b,** Tensile stress of SHP-3 at 100% strain with multiple cycles at 1000%/min with 15 minutes resting in between. SHP-3 which doesn't have UPy unit shows decrease of tensile stress indicating that UPy units impart the mechanical property. **c,** Residual strain measured by instron after 200% strain (holding time under strain: 0 h) with varying resting time. Self-healing materials for robust self-healing almost returned to its original state indicating the materials are elastic. **d,** Residual strain of SHP-3 measured by INSTRON after 200% strain (holding time under strain: 0 h) with varying resting time. SHP-3 doesn't return to its original state indicating that SHP-3 isn't elastic.

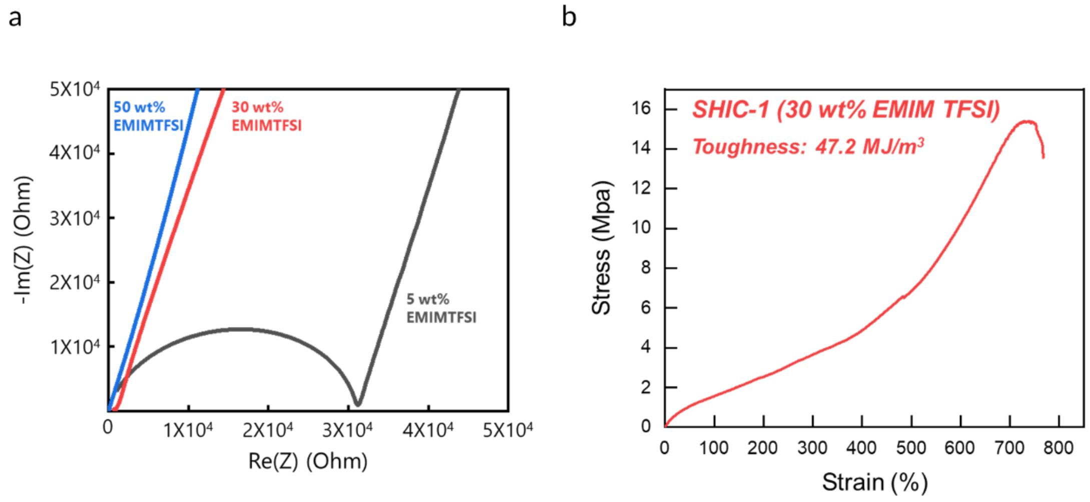

Supplementary Figure 12. Nyquist plot for SHIC-1 as a function of the amount of ionic liquid and the stress-strain curve (S-S curve) for SHIC-1 with 30 wt% EMIMTFSI.

a, The ionic conductivity value increased with the amount of added ionic liquid. SHIC with 5 wt% EMIMTFSI: 3.04×10^{-6} S/cm, SHIC with 30 wt% EMIMTFSI: 2.30×10^{-4} S/cm, SHIC with 50 wt% EMIMTFSI: 3.20×10^{-3} S/cm. **b,** SHIC with 30 wt% EMIMTFSI show tough mechanical property.

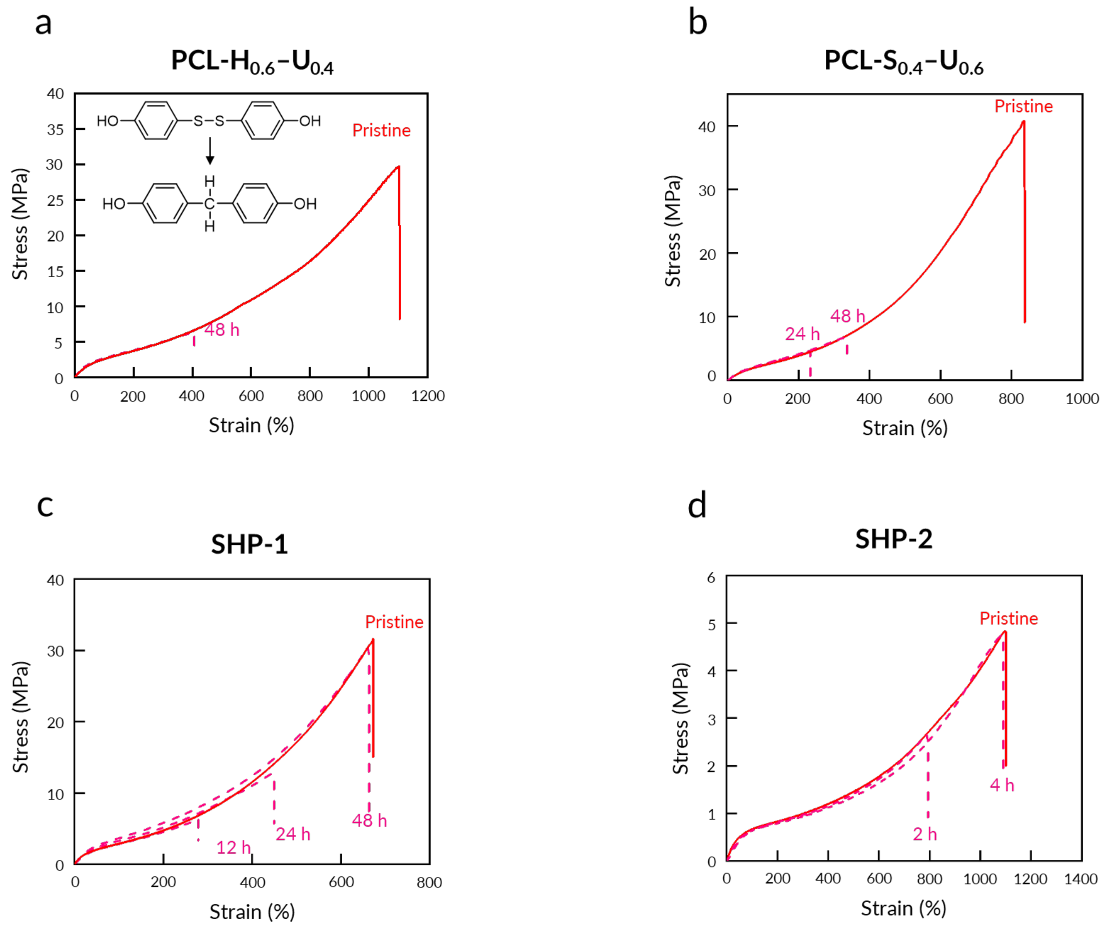

Supplementary Figure 13. Self-healing tests of materials.

Self-healing dog bone was cut into two pieces and then put any two pieces into contact. **a,** When 4,4’-dihydroxydiphenylmethane was used instead of bis(4-hydroxyphenyl) disulfide, the polymer was self-healed only 35% after 48 hours, indicating that disulfide imparts the self-healing properties of SHPs. **b,** PCL-$S_{0.4}$–$U_{0.6}$ was self-healed only 30% because strong because of restricted chain mobility for sef-healing. **c,** However, appropriate ratio of aromatic disulfide and UPy made complete self-healing. **d,** And SHP-2, which had a higher ratio of disulfide, was self-healed in a faster time.

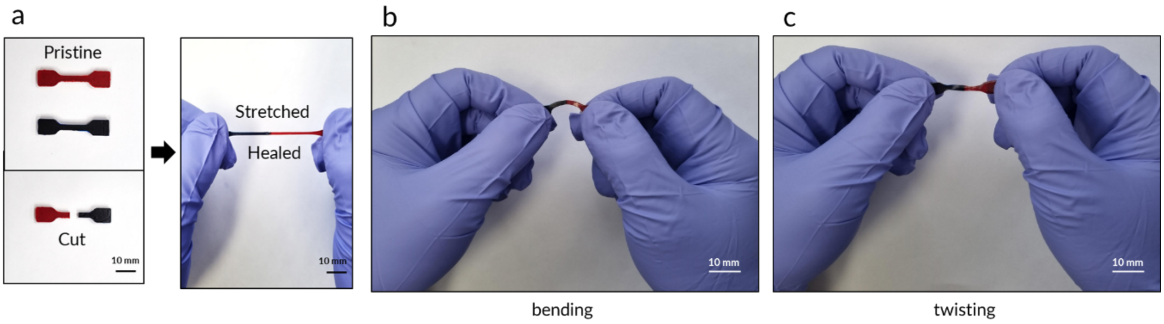

bending

twisting

Supplementary Figure 14. Self-healing tests of SHIC-1.

a, Dumbbell sample was bisected to two pieces and put together for self-healing. After some time, the jointed sample can be stretched, **b,** Bent and **c,** Twisted.

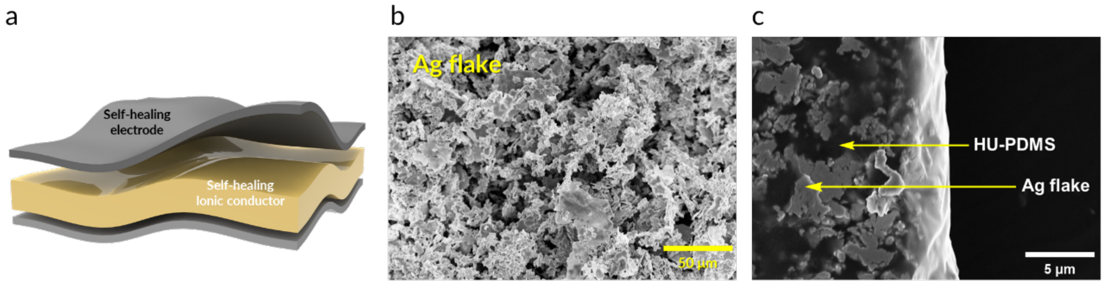

Supplementary Figure 15. Self-healing stretchable multimodal sensor and electrodes.

a, Schematic illustration of self-healing stretchable multimodal sensor. **b,** Scanning Electron Microscope (SEM) image of Ag flake. **c,** Scanning Electron Microscope (SEM) image of self-healing stretchable electrode.

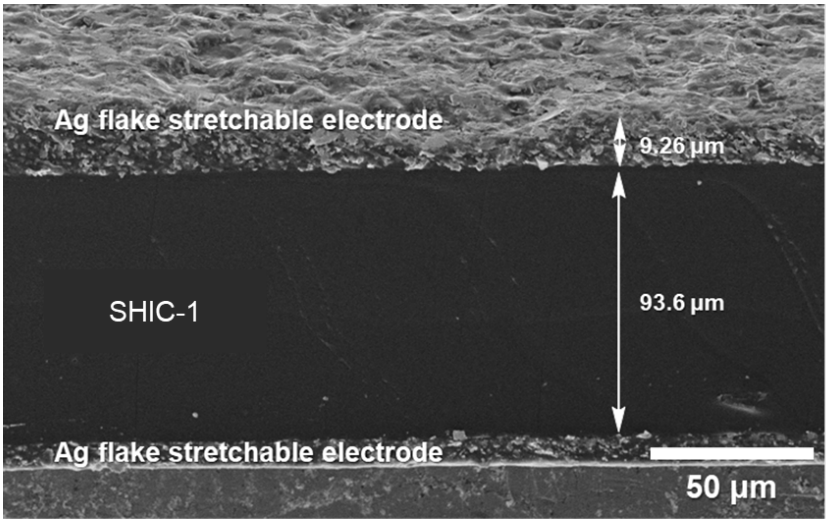

Supplementary Figure 16. SEM image of self-healing artificial multimodal sensor.

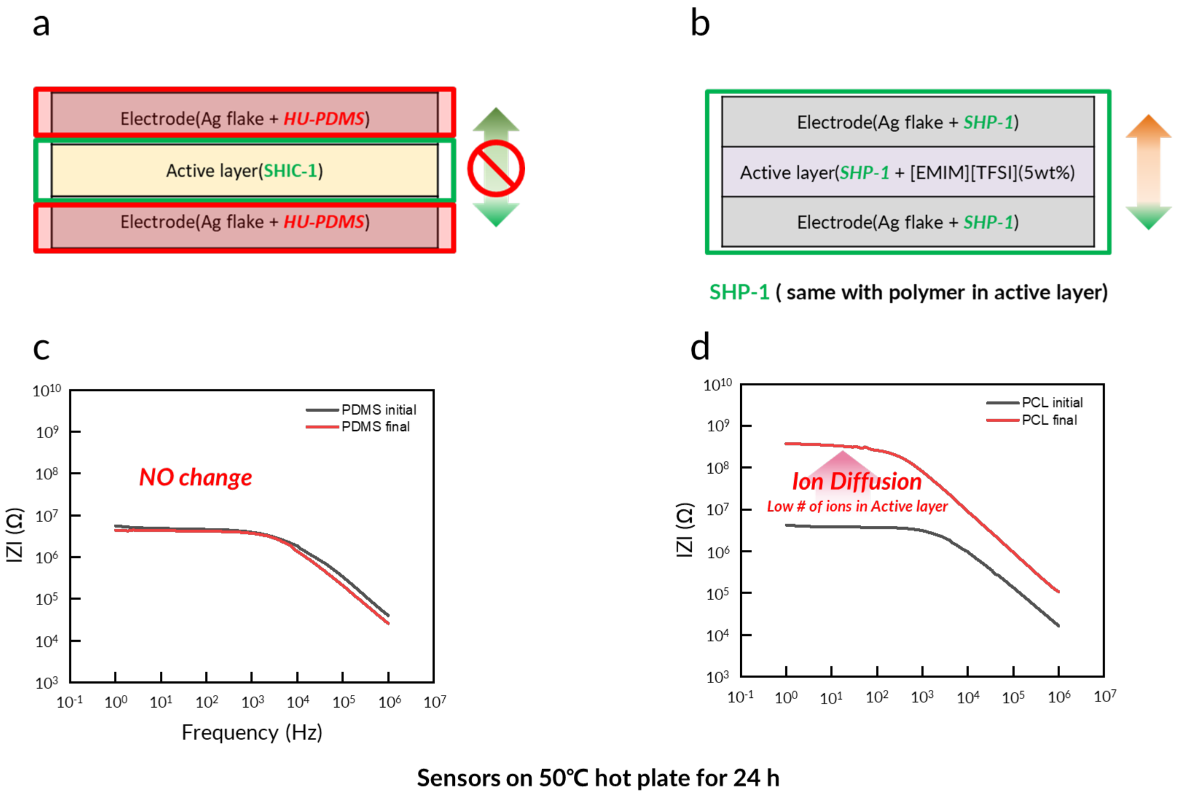

Supplementary Figure 17. A comparison between self-healing artificial multimodal sensors with different active layers.

a, Schematic illustration of self-healing multimodal sensor with electrodes composed of HU-PDMS and Ag. **b,** Schematic illustration of self-healing multimodal sensor with electrodes composed of SHP-1 and Ag. **c,** Because HU-PDMS was hydrophobic while PCL was hydrophilic, there was no significant change of impedance, after the sensors had been on 50 °C hot plate for 24 h. **d,** However, the recetor consisting of same polymer (PCL) showed dramatic change of impedance after the same process. So, the HU-PDMS with Ag flake was chosen for self-healing stretchable electrodes.

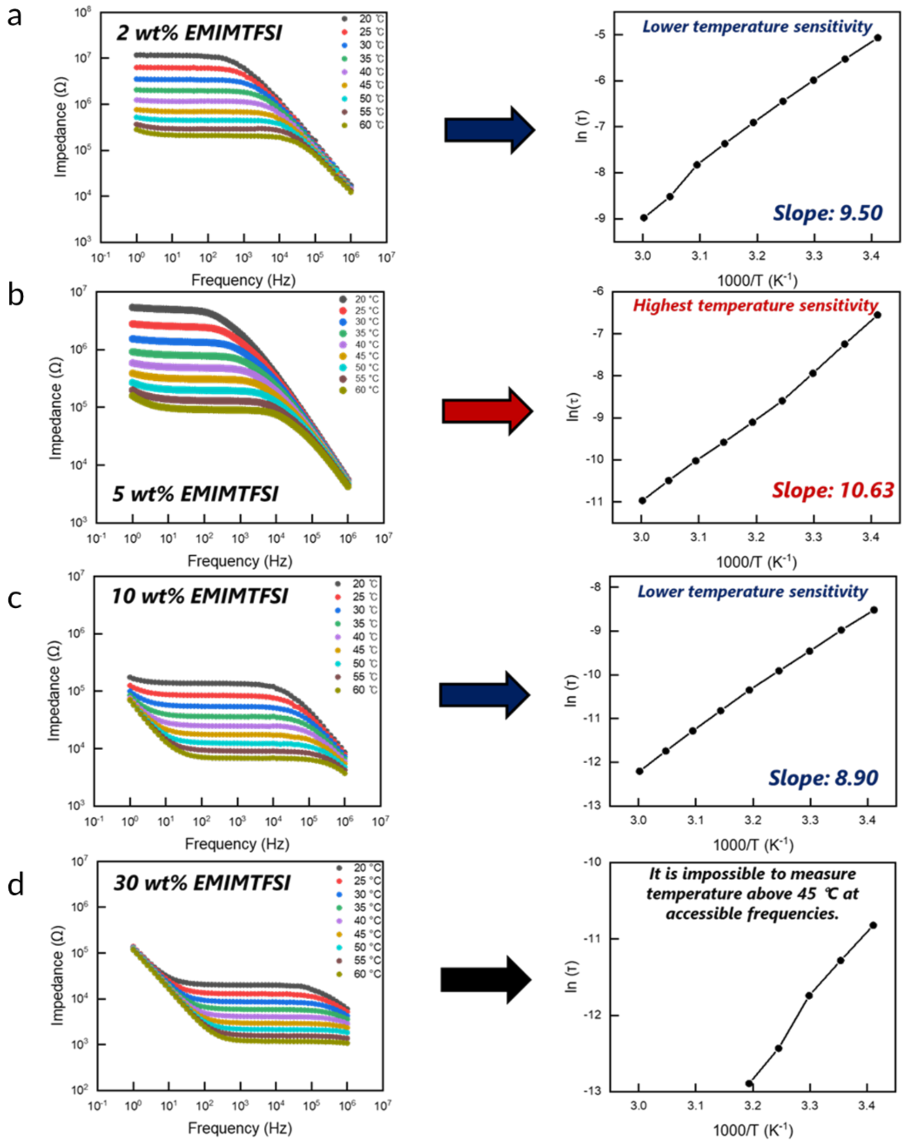

Supplementary Figure 18. Comparison of the temperature sensitivity of the multimodal sensor based on the amount of EMIMTFSI in the SHIC-1 active layer.

a, Bode plot for the multimodal sensor of SHIC-1 with 2 wt% EMIMTFSI used as the active layer. **b,** Bode plot for the multimodal sensor of SHIC-1 with 5 wt% EMIMTFSI used as the active layer. **c,** Bode plot for the multimodal sensor of SHIC-1 with 10 wt% EMIMTFSI used as the active layer. d, Bode plot for the multimodal sensor of SHIC-1 with 30 wt% EMIMTFSI used as the active layer.

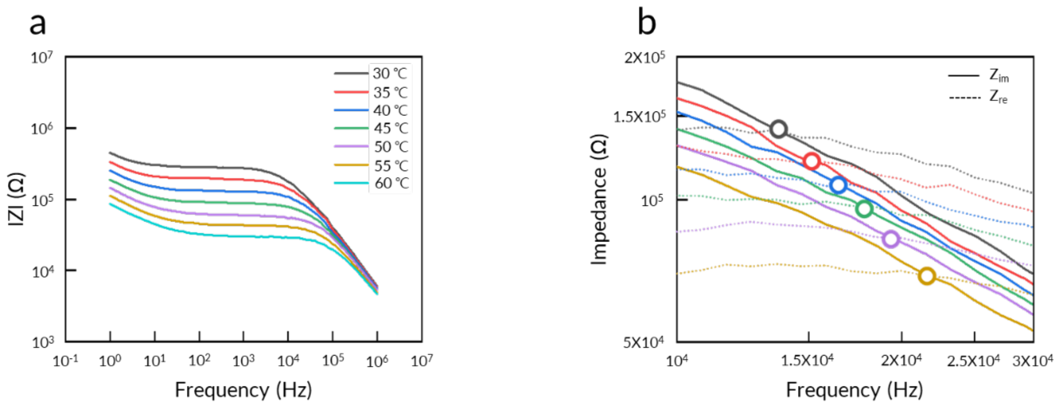

Supplementary Figure 19. Charge relaxation frequency behavior under different temperatures.

a, Bode plots with different temperatures. **b,** Charge relaxation frequency was depending on temperature.

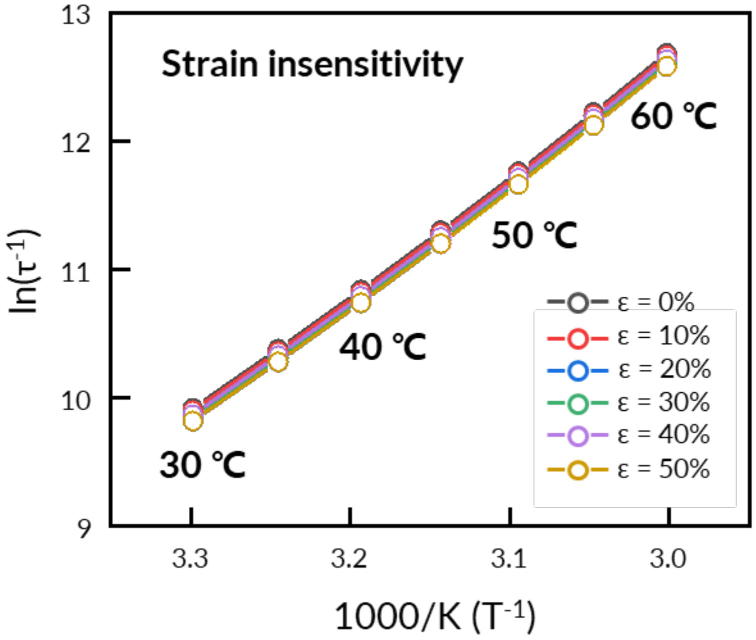

Supplementary Figure 20. Strain-insensitive temperature sensing under various temperature and strain.

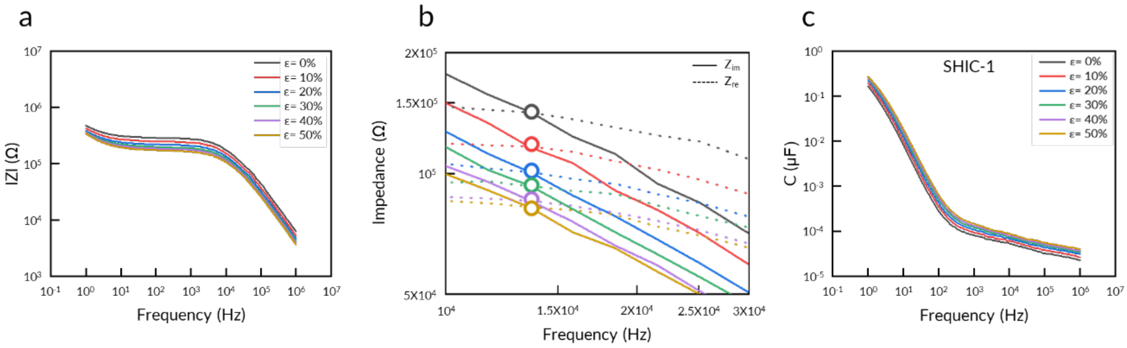

Supplementary Figure 21. Charge relaxation frequency and capacitance behavior under stretching.

a, Bode plots with different strains. **b,** Charge relaxation frequency showed constant values regardless of temperature, because charge relaxation frequency is an intrinsic variable. **c,** Capacitance in the same frequency changed according to strain, because the capacitance is an extrinsic variable that is sensitive to dimensional changes.

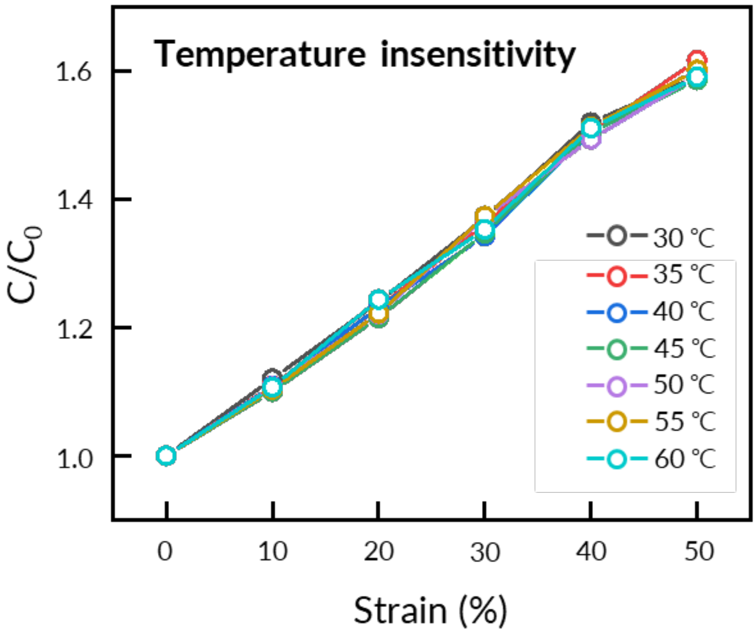

Supplementary Figure 22. Temperature-insensitive strain sensing under various temperatures and strains.

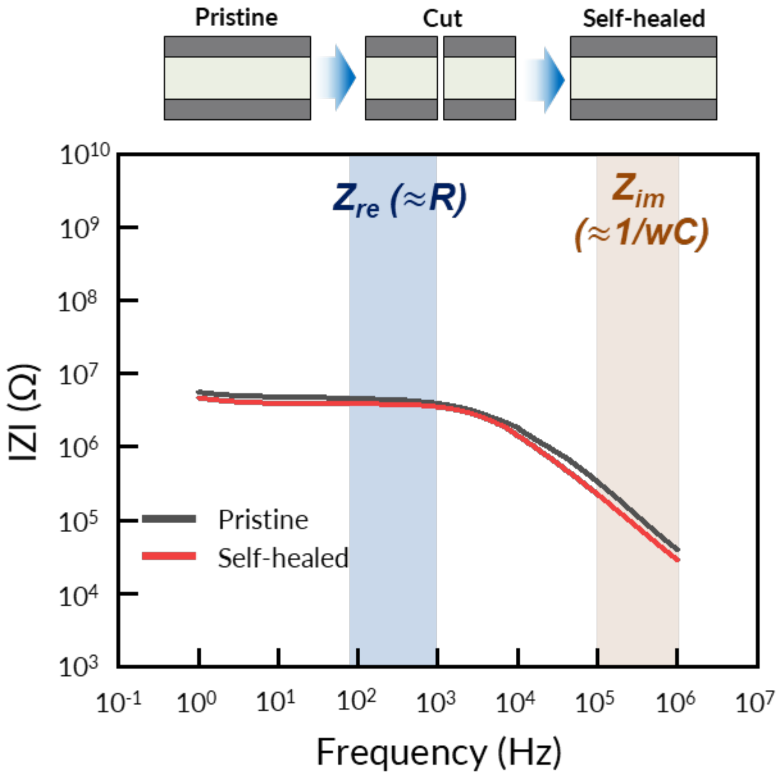

Supplementary Figure 23. Comparison of bode plots between pristine multimodal sensor and self-healed multimodal sensor.

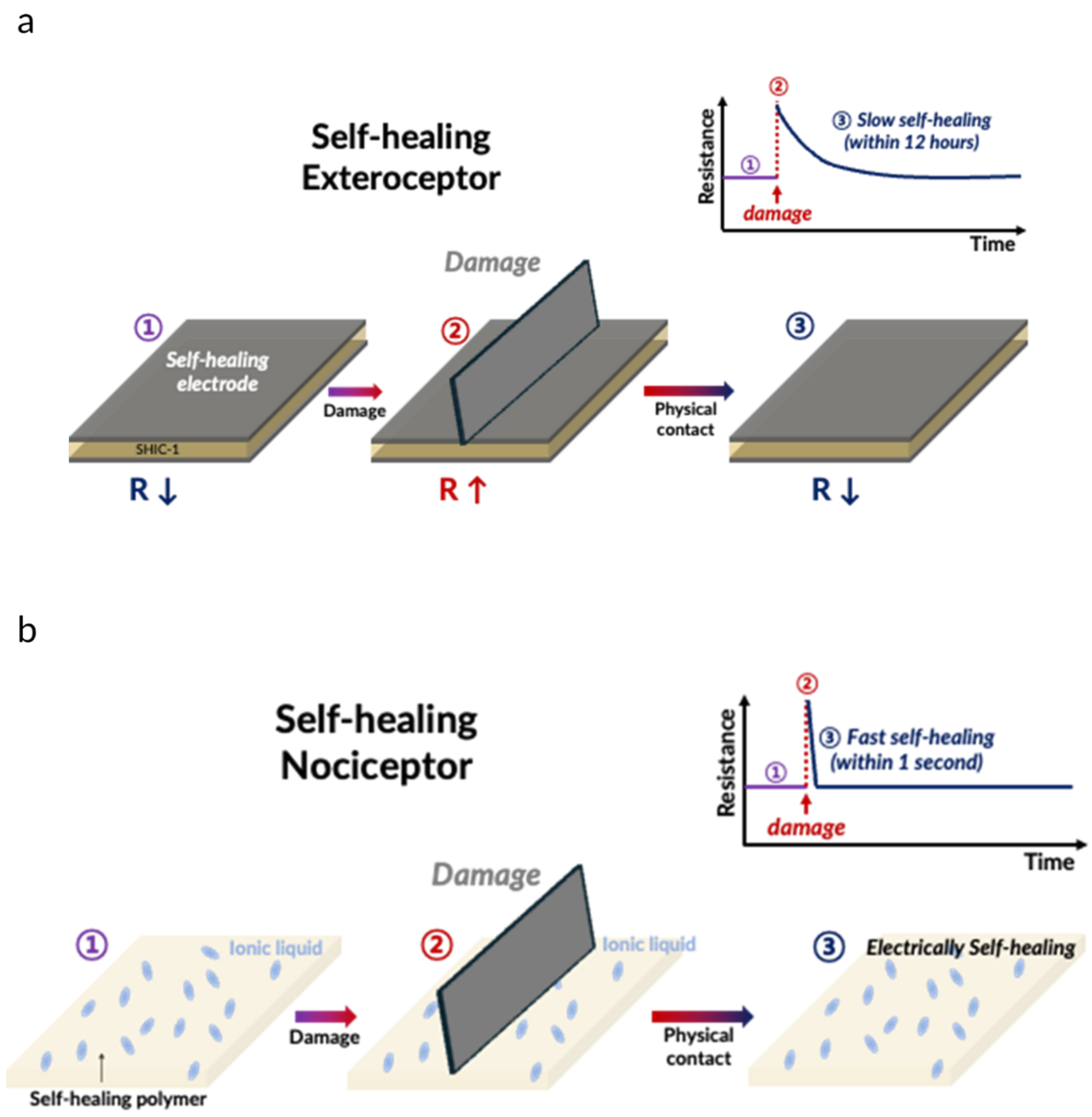

Supplementary Figure 24. Difference in self-healing speed between the self-healing multimodal sensor and the self-healing damage sensor.

a, In the case of the self-healing multimodal sensor, both the electrode and the active layer (SHIC with 5 wt% EMIMTFSI) need to undergo self-healing, resulting in a longer time for electrical self-healing. **b,** In contrast, the self-healing damage sensor, composed solely of SHIC-1, achieves self-healing more easily through physical contact. Additionally, due to the high concentration of ionic liquid (30 wt% EMIMTFSI), the self-healing speed is significantly faster.

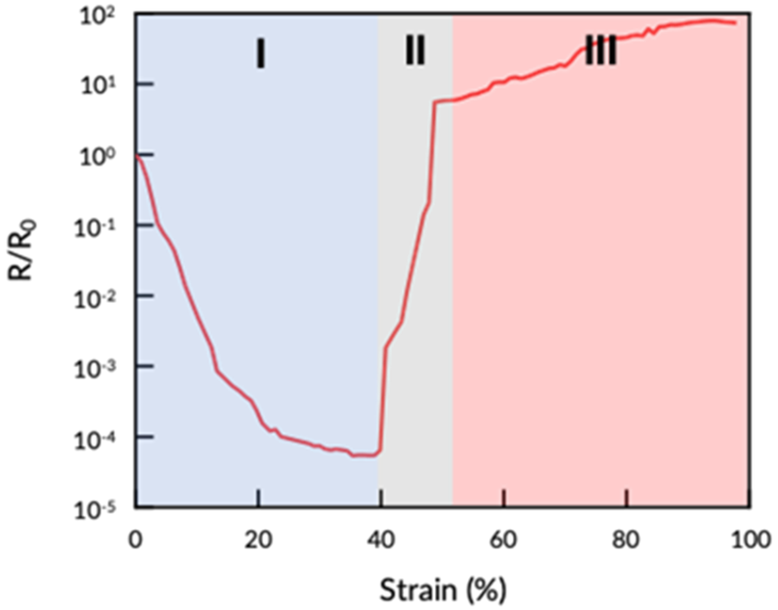

Supplementary Figure 25. Changes of resistance of flexion sensor as a function of strain.

At low levels of strain, micro-Ni particles of the flexion sensor form a conductive network, leading to a sharp decrease in resistance (I). Then, beyond a certain threshold of strain, the conductive network is disrupted, resulting in a rapid increase in resistance (II), ultimately a high resistance value (III). Consequently, when a soft gripper is actuated, a small strain is applied to the flexion sensor, causing a dramatical decrease in resistance.

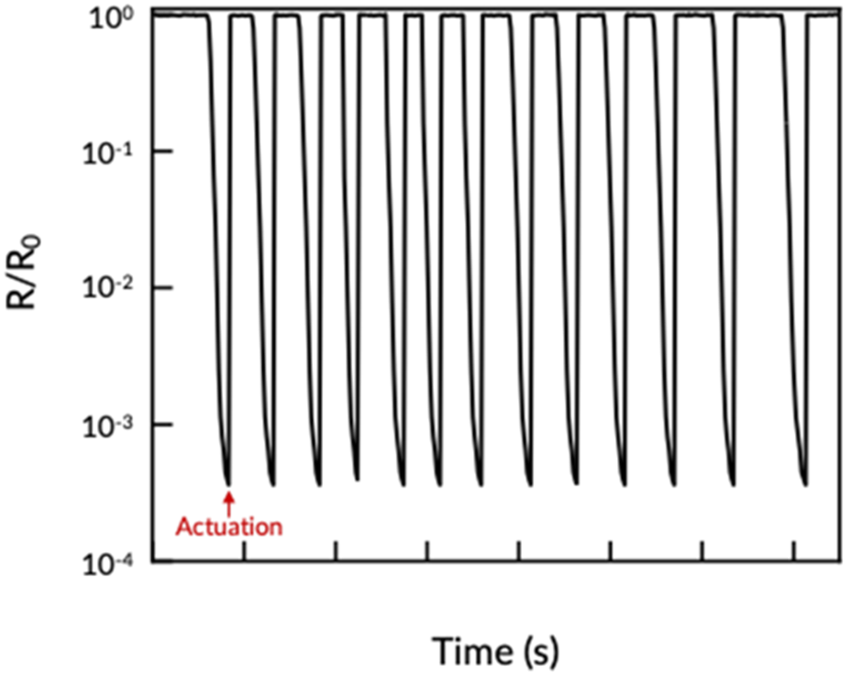

Supplementary Figure 26. Cyclic test of the flexion sensor.

It was confirmed that the flexion sensor exhibited consistent resistance changes when the soft gripper was actuated repeatedly.

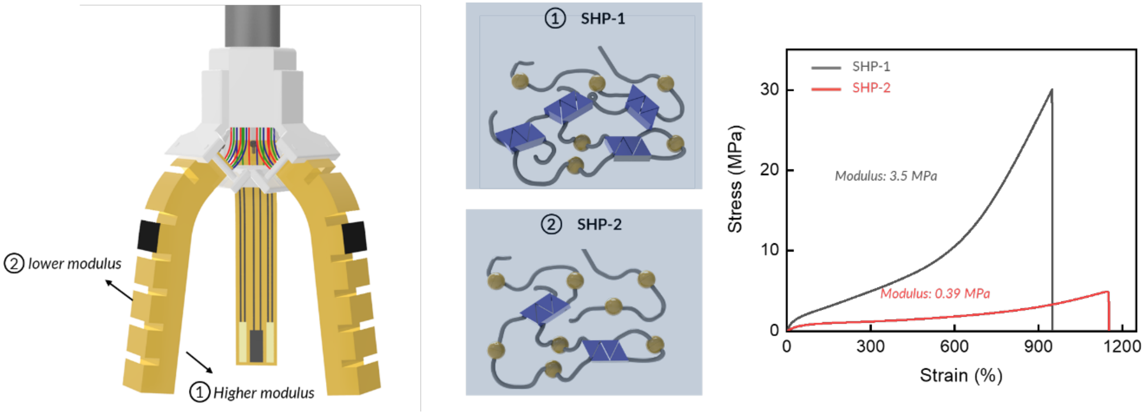

Supplementary Figure 27. The configuration of soft grippers.

For the soft gripper to function effectively under pneumatic pressure, there must be a modulus difference between the extensible layer and the inextensible layer. Therefore, SHP-2 with a low modulus was used for the extensible layer, while SHP-1 with a high modulus was used for the inextensible layer.

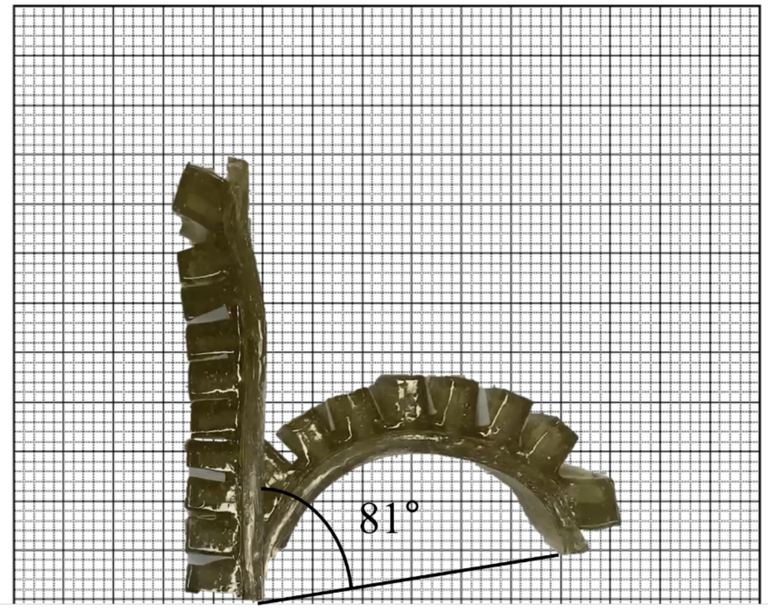

Supplementary Figure 28. Actuation ability of the self-healing gripper.

Supplementary Figure 29. Bending soft pneumatic actuator for soft gripper applications.

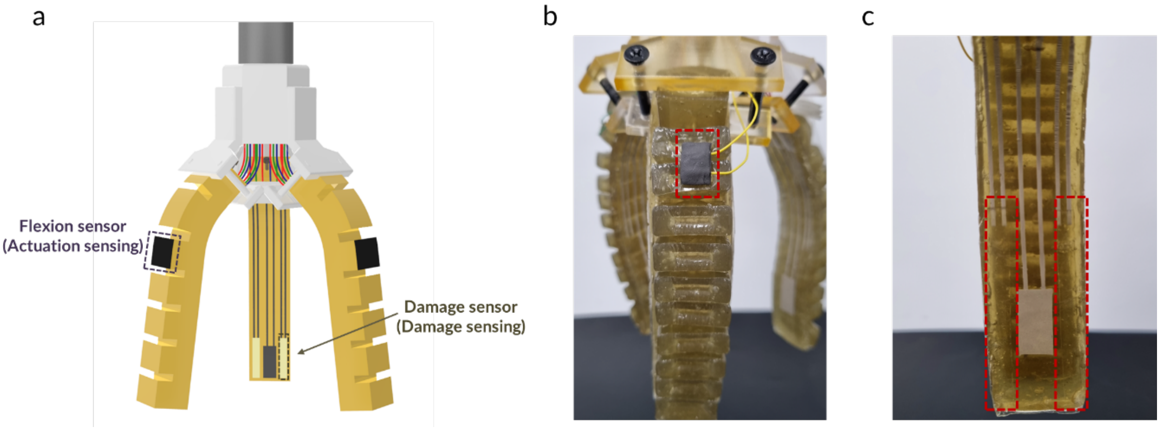

Supplementary Figure 30. Self-healing stretchable flexion sensor and damage sensor.

a, Schematic illustration of self-healing soft robots with flexion sensor and damage sensor. **b,** The photo of the flexion sensor. **c,** The photo of the damage sensor.

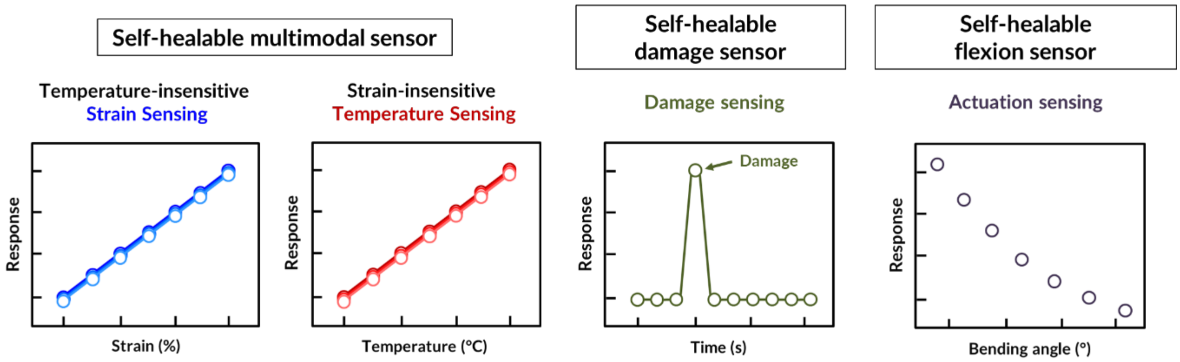

Supplementary Figure 31. Sensory systems of the soft robot.

Sensory systems are composed of self-healable multimodal sensor for tactile sensing, self-healable damage sensor for damage sensing, and self-healable flexion sensor for actuation sensing.

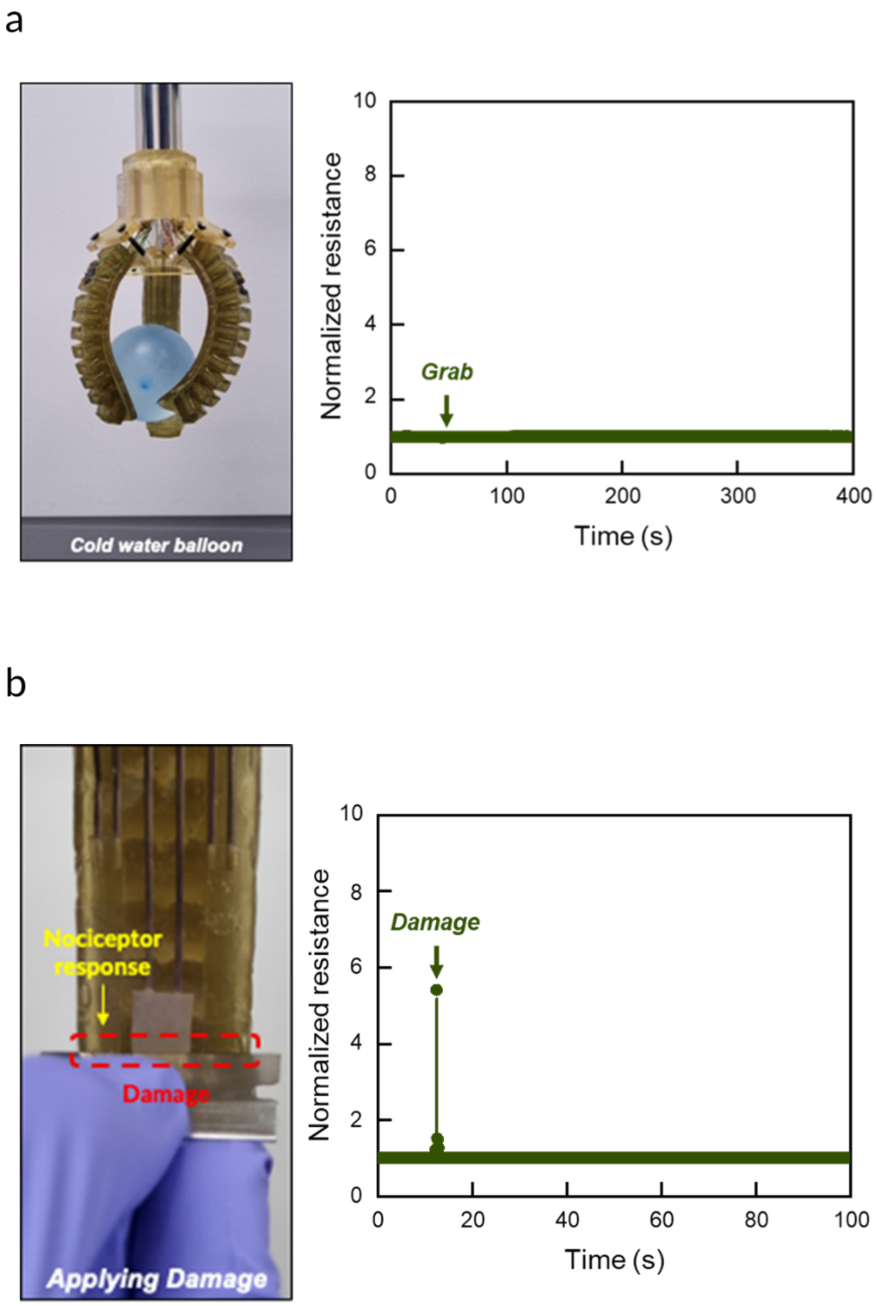

Supplementary Figure 32. Difference in resistance change of the self-healing damage sensor when grabbing an object versus when damage is inflicted.

a, When performing the action of grabbing an object, the resistance of the damage sensor remains almost unchanged. **b,** In contrast, when damage is inflicted, a significant resistance peak is observed. This experiment confirms that the damage sensor is responsive exclusively to damage.

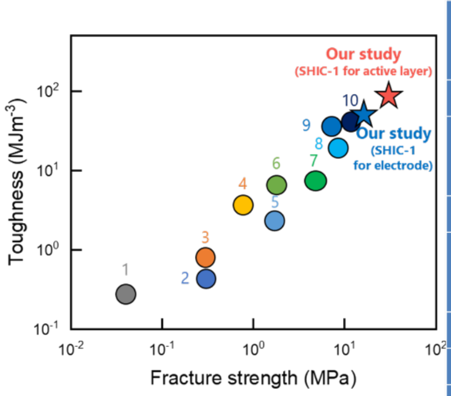

	Toughness	Fracture strength	Ionic conductivity	Application
1	0.04 MPa	0.28 MJ/m^{3}	10^{-3} S/cm	Strain sensor
2	0.3 MPa	0.45 MJ/m^{3}	-	-
3	0.3 MPa	0.8 MJ/m^{3}	1.2×10^{-3} S/cm	-
4	0.7 MPa	3.66 MJ/m^{3}	3.49×10^{-4} S/cm	Wearable sensor
5	1.6 MPa	2.4 MJ/m^{3}	4×10^{-3} S/cm	Strain sensor
6	1.75 MPa	6 MJ/m^{3}	10^{-4} S/cm	Flexible keyboard
7	5 MPa	7.5 MJ/m^{3}	2×10^{-3} S/cm	Strain sensor
8	8 MPa	20 MJ/m^{3}	4×10^{-5} S/cm	Triboelectric nano generator
9	7.5 MPa	35 MJ/m^{3}	10^{-4} S/cm	Strain sensor
10	12.6 MPa	45 MJ/m^{3}	-	-
SHIC-1 (active layer)	**30 MPa**	**87.3 MJ/m^{3}**	**3×10^{-6} S/cm**	**Stretchable multimodal sensor**
SHIC-1 (Electrode)	**15 MPa**	**47.2 MJ/m^{3}**	**2.3×10^{-4} S/cm**	**Damage sensor**

#	References
1	Zhang, L. et al. Self-Healing, Adhesive, and Highly Stretchable Ionogel as a Strain Sensor for Extremely Large Deformation. *Small.* **15**, 1804651 (2019).
2	Kaimo, E., Yasui, T., Iida, Y., Gong, J. & Matsuyama, H. Inorganic / Organic Double-Network Gels Containing Ionic Liquids. *Adv. Mater.* **29**, 1704118 (2017).
3	Tamate, R. et al. Self-Healing Micellar Ion Gels Based on Multiple Hydrogen Bonding. *Adv. Mater.* **30**, 1802792 (2018).
4	Xu, L. et al. A transparent, Highly Stretchable, Solvent-Resistant, Recyclable Multifunctional Ionogel with Underwater Self-healing and Adhesion for Reliable Strain Sensors. *Adv. Mater.* **33**, 2105306 (2021).
5	Xu, J., Wang, H., Du, X., Cheng, X., Du, Z. & Wang, H. Self-healing, anti-freezing and highly stretchable polyurethane ionogel as ionic skin for wireless strain sensing. *Chemical Engineering Journal.* **426**, 130724 (2021).
6	Yang, L. et al. Mechanically Robust and Room Temperature Self-healing Ionogel Based on Ionic Liquid Inhibited Reversible Reaction of Disulfide Bonds. *Adv. Sci.* **10**, 2207527 (2023).
7	Xu, J., Wang, H., Wen, X., Wang, S. & Wang, H. Mechanically Strong, Wet Adhesive, and Self-Healing Polyurethane Ionogel Enhanced with a Semi-interpenetrating Network for Underwater Motion Detection. ACS. *Appl. Mater. Interfaces.* **14**, 54203-54214 (2022).
8	Li, H., Xu, F., Guan, T., Li, Y. & Sun, J. Mechanically and environmentally stable triboelectric nanogenerator based on high-strength and anti-compression self-healing ionogel. *Nano Energy.* **90**, 106645 (2021).
9	Zhang, M. et al. Self-healing, mechanically robust, 3D printable ionogel for highly sensitive and long-term reliable ionotronics. J. Mater. Chem. A. 10, 12005-12015 (2022).
10	Wang, M et al. Tough and stretchable ionogels by in situ phase separation. *Nat. Mater.* **21**, 359-365 (2022).

Supplementary Table 1. Comparison of the ionic conductivity and mechanical toughness of ionic conductors mentioned in the references.